Revision 1:

Decrease of hydrogen incorporation in forsterite from CO_2-H_2O-rich kimberlitic liquid

Virginie Baptiste[1*], Sylvie Demouchy[1], Shantanu Keshav[1], Fleurice Parat[1], Nathalie Bolfan-Casanova[2], Pierre Condamine[2], & Patrick Cordier [3]

[1]*Géosciences Montpellier, Université Montpellier & CNRS, CC 60, Place E. Bataillon, 34095 Montpellier cedex 5, France.*

[2] *Laboratoire Magmas et Volcans, CNRS, 5, rue Kessler, 63000 Clermont-Ferrand, France*

[3] *Unité Matériaux et Transformation, Université Lille 1 & CNRS, UMR 8207, Villeneuve d'Ascq, France.*

Running title: Decrease of H incorporation in forsterite from CO_2-H_2O-rich kimberlitic liquid

Revised version for Am. Min.

(*) corresponding author: virginie.baptiste@gm.univ-montp2.fr;

Phone: +33 467144912

Fax: +33 467143603

Abstract

To test if hydrogen incorporation by ionic diffusion can occur between a volatile-rich kimberlitic liquid and forsterite, results of high pressure, high temperature experiments using a piston-cylinder apparatus at 1200-1300°C and 1 GPa for durations of 1 min, 5h, and 23h, are reported here. Kimberlitic liquid in the system CaO-MgO-Al_2O_3-SiO_2-CO_2-H_2O and synthetic forsterite single crystals were chosen as a first simplification of the complex natural kimberlite composition. Unpolarized Fourier transform infrared spectroscopy was used to quantify the concentrations of OH in the crystallographically oriented forsterite. Scanning electron microscopy, electron backscattered diffraction, electron microprobe analysis, and transmission electron microscopy were performed to identify the run products. After 5h and 23h, a forsterite overgrowth crystallized with the same orientation as the initial forsterite single crystal. The kimberlitic liquid has crystallized as micron-scale euhedral forsterite neocrystals with random crystallographic orientations, as well as a nano-scale aluminous phase and a calcic phase. Despite theoretical water-saturation of the system and long duration, none of the initial forsterite single crystals display signs of hydration such as hydrogen diffusion profile from the border toward the center of the crystal. Most likely, the presence of CO_2 in the system has lowered the H_2O fugacity to such an extent that there is no significant hydration of the starting forsterite single crystal or its overgrowth. Also, CO_2 has enhanced rapid forsterite crystal growth. Forsterite growth rate is around 2 x10^8 μm^3/h at 1250°C. These experimental results suggest a deep mantle origin of the high OH content found in natural mantle-derived xenoliths transported in kimberlites, as reported from the Kaapvaal craton. In agreement with previous studies, it also points out to the fact that significant hydration must take place in a CO_2-poor environment.

Keywords: Kimberlite, water, hydrogen, diffusion, olivine, point defect.

Introduction

Incorporation of hydrogen in nominally anhydrous minerals (NAMs), even at trace concentrations (ppm by weight level), is known to have a significant impact on the chemical and physical properties of the rocks and minerals in Earth's mantle such as melting temperature, electrical conductivity, seismic velocities, and rheology (e.g., Karato et al., 1990; Mackwell et al., 1985; Hirth and Kohlstedt, 1996; Demouchy et al., 2012; Gaetani and Grove, 1998; Jacobsen et al., 2008). For instance, in terms of rheology, olivine controls the viscosity of the lithosphere root. The low OH^- concentrations (< 20 ppm H_2O wt, with concentration calculated using the FTIR calibration of Paterson, 1982) of olivine have been proposed to increase the mantle viscosity of the South African craton, and hence could be responsible for its longevity (Peslier et al., 2010; Baptiste et al., 2012). To test if it is also the case for other cratons, concentration of hydrogen was recently measure in mantle peridotites from the Siberian craton, but the results have not confirmed the observation of the South African craton (Doucet et al., 2014). Prior to these recent studies, several publications have reported high concentrations of OH (> 30 ppm H_2O wt) in olivine from mantle xenoliths, olivine megacrysts, and kimberlitic olivine phenocrysts from several cratons (e.g., South Africa, Siberia, and Canada; see Miller et al., 1987; Matsyuk et al., 1998; Bell et al., 2004; Matsyuk and Langer, 2004; Kamenetsky et al., 2008; Peslier et al., 2010; Peslier, 2010, Doucet et al., 2014). In particular, relatively high concentrations of OH in olivine (up to 150 ppm H_2O wt) have been reported in olivine of mantle xenoliths from the Kaapvaal craton (Peslier et al., 2010; Baptiste et al., 2012), except for the deepest samples, which are almost anhydrous (<10 ppm H_2O wt). Further, high concentrations of OH in olivine

(54-419 ppm H_2O wt) have been measured in megacrysts and macrocrysts from kimberlites (Bell et al., 2004, Matsyuk and Langer, 2004; Matveev and Stachel, 2007) suggesting that kimberlite would be a favorable environment for important hydrogen incorporation in olivine.

Studies on Kaapvaal mantle xenoliths usually report homogeneous OH concentration profiles across olivine grains suggesting the absence of hydration or dehydration process caught-in-the-act (Peslier et al., 2010; Baptiste et al., 2012). However, the origin of hydrogen in olivines from the cratonic mantle still remains unclear. High concentration of OH in olivine in Kaapvaal xenoliths could have been inherited from (1) metasomatism, if water-saturated fluids or water-saturated percolating melts impregnated the cratonic root, or (2) during transport by the volatiles-rich (mostly CO_2 and H_2O) kimberlitic magmas (Brooker et al., 2011; Baptiste et al., 2012). Yet, so far, experimental studies have not tested the second hypothesis or quantified the diffusion of hydrogen between a volatile-rich kimberlitic melt/magma and olivine.

The aim of this study is to test if hydrogen incorporation by ionic diffusion can occur between a model volatile-rich kimberlitic liquid in the system CaO-MgO-Al_2O_3-SiO_2-CO_2-H_2O ($CMAS$-CO_2-H_2O) and iron-free forsterite at high pressure and temperature during transport toward the surface.

Sample preparation and experimental method

A synthetic volatile-rich kimberlite starting material was prepared with high purity oxides (SiO_2 - Aldrich, 99.995%, Al_2O_3 - Alfa Aesar, 99.998%, MgO - Alfa Aesar, 99.998%), high purity calcium carbonate ($CaCO_3$ - Alfa Aesar, 99.998%), magnesium hydroxide (brucite, $Mg(OH)_2$ - Alfa Aesar, 99.998%), and a very pure natural magnesite ($MgCO_3$) from Oberdorf (Austria, see Buob et al., 2006). The silicate portion of the starting mixture was prepared first. The components MgO, Al_2O_3, and SiO_2 were fired in platinum (Pt) crucibles for at least 18-20

hours in air at 1250°C, and $CaCO_3$ at 400°C. Pt crucibles were used that had not been previously utilized to dry either iron metal or iron oxides. Afterwards, the fired oxides and $CaCO_3$ were immediately mixed in appropriate proportions, and ground for at least 1 hour under ethanol in an agate mortar. After drying under an infrared (IR) heat lamp, the mixture was decarbonated in air in a high temperature, room pressure furnace. To decarbonate, the temperature of the furnace was slowly ramped to 1000°C over 10 hours, and maintained at this temperature for 6-7 hours. After this step, the mixture was taken out of the furnace, and then transferred to another high temperature furnace to prepare a glass by melting the mixture in air at 1650°C for about 4 hours. To quench this liquid to a glass, the Pt-crucible containing the mixture was partially immersed in an ice-water bath, and the resulting glass was optically clear and transparent. This glass was finely ground under ethanol for about 30-40 minutes, and using the same procedure, glassing was repeated twice more. To ensure homogeneity, the silicate glass was then re-ground for 1 hour under ethanol in an agate mortar, and then dried under an IR heat lamp for about 1 hour. Finally, CO_2 and H_2O were added in the silicate glass as magnesite and brucite, respectively. Ground magnesite and brucite were fired at 250°C and 120°C, respectively in air in a Pt-crucible for over 17 hours, to obtain stoichiometric components, then mixed and ground with the silicate glass in an agate mortar under ethanol for another 1 hour. The final powder was stored in a desiccator. The composition of this starting composition is reported in Table 1 and was designed on the basis of published compositions of: (1) erupted kimberlites (Smith et al., 1985a, b; Mitchell, 1986, 1995; Becker and Le Roex, 2006; Kamenetsky et al., 2008; Kjarsgaard et al., 2009; Sparks et al., 2009, Brooker et al., 2011), (2) the results of experimental petrology of kimberlites in the system CMAS-CO_2 (Dalton and Presnall, 1998; Gudfinnsson and Presnall, 2005), and (3) the solubility of water (H_2O) in model carbonatitic melts (Keppler, 2003). From studies in the system CMAS-CO_2 (e.g., Gudfinnsson and Presnall, 2005), it appears that kimberlites are not stable liquids at 1

GPa, but at higher pressures >5 GPa (Gudfinnsson and Presnall, 2005). At such high pressures, the liquid used here will be in equilibrium with forsterite, orthopyroxene (opx), clinopyroxene (cpx), and garnet (Gudfinnsson and Presnall, 2005). Here, the starting composition was chosen to target hydration of olivine from kimberlite liquid during transport toward the surface (e.g., then in a rising metastable kimberlitic liquid), and accordingly, the experiments were run at a lower pressure than their estimated depth of genesis, on the basis of previous experimental petrology studies (Dalton and Presnall, 1998; Gudfinnsson and Presnall, 2005).

Crystallographically oriented iron-free forsterite, from the company Roditi, was used in the experiments. Original crystallographic orientation provided by Roditi was checked and confirmed using polarized FTIR and using Si-O bands. All the experiments reported here were performed at Laboratoire Magmas et Volcans, Clermont-Ferrand (France). High pressure assemblies were prepared by placing a crystallographically oriented single crystal of forsterite within ~60 mg of the kimberlitic starting material, in 4 mm outer diameter and 7 mm length gold-palladium ($Au_{75}Pd_{25}$; simply AuPd from now on) capsules (see Fig. 1), which were then welded. AuPd capsules were chosen to minimize water loss. Single crystals of forsterite were on average $2.20 \times 2.65 \times 1.9$ mm in dimensions (for [100], [010], and [001] being the crystallographic axes, respectively). The capsules were then placed in salt (NaCl) cylinders. Experiments were performed in a 19.1 mm non end-loaded piston cylinder apparatus (pressure calibrations detailed in Xirouchakis et al., 2001). Temperature was controlled using a $W_{74}Re_{26}$-$W_{95}Re_5$ thermocouple. Five runs at 1 GPa were annealed at 1200°C for 1 min, 5h and 23h, or annealed at 1250 and 1300°C for 5h. Annealing duration over 2 hours at temperature above 900 °C is long enough to permit detectable hydrogenation of olivine or forsterite, including diffusion profile (Demouchy and Mackwell, 2003, 2006) at pressures above 0.2 GPa. Temperature quench rate was $50°C.s^{-1}$.

Experimental conditions are summarized in Table 2. Short duration experiments (<100 h) were chosen to avoid significant hydrogen loss or reaction with the capsule (<50h). The experimental duration of 1 min was chosen to test if significant hydrogen diffusion between the forsterite crystal and kimberlitic liquid occurred while heating the experimental charge. After experimental runs, each capsule was pierced to check for excess free fluid to ensure or negate fluid-saturation of the liquid; each capsule had visibly escaping fluid bubbles.

Sample analysis

Electron microprobe analysis (EMPA)

Major element composition of the forsterite crystals was determined before the experiments using a Cameca SX100 electron microprobe at the Microsonde Sud facility, in Montpellier (France). Analytical conditions were a focused beam of 20 kV of accelerating voltage and 10 nA probe current at the Faraday cup. After experimental runs, the compositions of the forsterite crystal and the newly formed phases were also determined. Results are reported in Table 1. Typical composition of natural Group-I and Group-II kimberlites from Becker and Le Roex (2006) are also provided for comparison.

Fourier transform infrared spectroscopy

Each capsule was doubly hand-polished for unpolarized Fourier transform infrared spectroscopy (FTIR) analysis. The capsule sections were immersed in pure acetone for at least 12h to dissolve any intergranular CrystalBond glue before analysis. FTIR spectroscopy analyses were performed at the Laboratoire des Colloïdes, Verres, Nanomatériaux in Montpellier (France) using a Bruker IFS66v coupled with a HYPERION 3000 Bruker microscope and a liquid

nitrogen-cooled mercury-cadmium-telluride (MCT) detector. A Globar light source and a Ge-KBr beam splitter were used to generate unpolarized mid-infrared radiation. A background measurement was performed before analysis. Measurements were acquired with a squared aperture yielding a squared beam spot between 30 and 100 μm, with the IR beam being parallel to [010] crystallographic axis of the forsterite crystals and on a [100]-[001] plane (i.e., across the basal plane of the capsule). Two hundred scans were accumulated with a resolution of 4 cm^{-1} for each measurement. A baseline correction was applied on each spectrum using the OPUS software. Spectra were then normalized to a sample thickness of 1 cm. Fractures and inclusions were strictly avoided. The sample thickness was measured using a micrometer with an accuracy of ± 1 μm. The calibration of Paterson (1982) was used to quantify the concentration of OH in forsterite:

$$C_{OH} = \frac{X_i}{150\zeta} \int \frac{k(\bar{\nu})}{(3780 - \bar{\nu})} d\bar{\nu} \qquad \text{eq.1}$$

where C_{OH} is the hydroxyl concentration (in mol H/l), ζ is an orientation factor (1/3 for unpolarized measurements), and $k(\bar{\nu})$ is the absorption coefficient in cm^{-1} for a given wavenumber $\bar{\nu}$. Xi is a density factor equal to 2750 ppm H_2O wt, for iron-free forsterite (for the calculation method, see Bolfan-Casanova et al., 2000). For a given thickness of the forsterite sample, the detection limit of FTIR spectroscopy is 0.5 ppm H_2O wt, and uncertainty on the hydrogen concentration is ± 15% (Demouchy and Mackwell, 2003).

Scanning electron microscopy and electron backscattered diffraction

After experimental runs, section cut through VB6 and VB12 capsules were mounted on epoxy plugs and carefully polished. Analyses were performed with a scanning electron microscope (SEM) CamScan X500FE CrystalProbe equipped with an electron backscattered

diffractometer (EBSD) at Geosciences Montpellier (France), using an acceleration voltage of 25kV and a working distance of 20 mm. To avoid charging of the samples, low vacuum conditions were chosen (5 Pa of gaseous nitrogen). EBSD patterns were produced by interaction between an electron beam at 20° to the horizontal sample stage (see Demouchy et al. 2011 for a detailed description of the CrystalProbe-EBSD). Data were acquired using CHANNEL5 software. Punctual measurements were made to determine the crystallographic orientation of the forsterite single crystals and the newly produced crystalline phases.

Transmission electron microscopy.

Transmission electron microscopy (TEM) was used to identify nano-scale mineral phases within the forsterite overgrowth. After SEM-EBSD, a VB6 basal section was cut in half. Focused ion beam technique (FIB) was used to extract two electron-transparent samples from the overgrowth region. TEM investigations were performed in Lille (France) with a FEI® Tecnaï $G^2$20Twin microscope, operating at 200 kV with a LaB_6 filament. Precession electron diffraction was performed in the selected area mode using a "Spinning Star" precession module from the Nanomegas company. Elemental distributions were obtained in the TEM by EDS X-ray intensity maps, using spectral imaging wherein each pixel of a spectrum image contains a full EDS spectrum mode. Spectrum images were acquired in the Scanning Transmission Electron Microscopy (STEM) mode.

Results

Results from SEM-EBSD are presented first, followed by the characterization using EMPA, TEM-EELS and finally FTIR results. SEM images of the typical recovered capsule are

shown in Fig. 2. During the experiments, the original shape of the forsterite single crystal has been largely well preserved; yet, due to decompression, few fractures developed. Micrometer-size forsterite overgrowths, which formed, display the same crystallographic orientation (homo-epitaxy) as the initial forsterite single crystal as shown by the Kikuchi bands pattern in Fig. 3a and 3b. The size of the forsterite overgrowth increases with increasing run duration and reaches up to 135 microns after 23h. In addition, the kimberlitic melt has crystallized euhedral neocrystals of forsterite with variable crystallographic orientations as shown in Figs. 2c and 3. From EBSD and Energy Dispersive X-ray (EDX), a minor spinel-like (cubic) Al-rich crystalline phase was also identified, occurring mostly as small crystallites (tens of nanometers) within the forsterite overgrowth as shown in Fig. 2e, and by point analysis in Fig. 3d. A Ca-rich phase with well-defined crystallographic planes has also been identified (Fig. 2, and 3e). Several vesicles were present (20 μm in diameter), but glass was not observed.

Subsequent EMPA analyses (Table 1) reveal that the forsterite single crystal, forsterite overgrowths, and the forsterite neocrystals have very similar major element composition; although the forsterite overgrowths and the forsterite neocrystals are slightly enriched in Ca (0.43-0.31 wt.% CaO, Table 1). The Al-rich phase has a composition closer to spinel than sapphirine and corundum (Ackermand et al., 1975), but is enriched in CaO (>10 wt.%), an unavoidable consequence of beam overlap between the very small Al-rich and the Ca-rich phases. The Ca-rich phase has a composition close to monticellite ($CaMgSiO_4$, Deer et al., 1992, p354-355; Brooker et al., 2011) but with lower silica content; the possibility that it could be a carbonate-like phase as well (probably calcite) cannot be disregarded. For both the Al-rich and Ca-rich phases, the size of the phases (below 10 nanometers) has significantly limited the quality of the EMPA analyses, and thus proper phase identification.

TEM-EDX analyses confirm the occurrence of Al-rich spinel, a Ca- and C- rich and SiO_2 poor nano-scale mineral phase (carbonate-like) as illustrated in the TEM-EDX map in Fig. 4. The slight enrichment in Ca of forsterite overgrowth (Table 1) is confirmed as well by TEM-EDX spectra.

FTIR analyses were performed on post-run forsterite single crystals (center and border) as well as on the adjacent forsterite overgrowths. The unpolarized border spectra are displayed in Fig. 5 and 6. For the same border position in the forsterite single crystal, the FTIR spectra neither change as a function of temperature/experimental duration (Fig. 5), nor display significant absorption bands within the OH absorption field in forsterite. Only a very weak band at 3350 cm^{-1} in VB10 is observed (Fig. 5) in the forsterite single crystal and a minor OH band at 3612 cm^{-1} in VB12 in the forsterite overgrowths (Fig. 6). These minor bands at 3350 cm^{-1} and 3612 cm^{-1} are characteristic of iron-free forsterite (Demouchy and Mackwell, 2003, Lemaire et al., 2004), and the large broad band at 3427 cm^{-1} has been previously attributed to inter-granular water (e.g., Keppler and Rauch, 2000; Demouchy et al., 2012). The calculated concentration of OH in the forsterite samples does not exceed 2 ppm H_2O wt. (Fig. 5 and Table 2). The main absorption band at 3698 cm^{-1} recorded by the FTIR spectra measured in the forsterite overgrowth as well as in the surrounding matrix is attributed to serpentine (Miller et al., 1987) or brucite, and is not typical of the OH IR band in forsterite. The amplitude of these bands increases with increasing distance away from the interface as the vertical beam path (i.e., the convergent beam is a square of 50 microns in the focus plane) includes more and more matrix material and less forsterite single crystal. In the next section, we discuss the lack of significant hydration of the forsterite single crystal and the possible consequences for the hydration mechanism of the lithospheric mantle.

Discussion

Effect of CO_2 on OH solubility in forsterite

Unpolarized FTIR analyses have demonstrated that despite the use of a H_2O-rich system and long duration, none of the forsterite single crystals display signs of typical hydration at OH saturation level or significant diffusion profile of OH from the border toward the center of the crystal. Furthermore, FTIR spectra and absorption level measured in the forsterite do not match the forsterite spectra from hydration experiments at high pressure and temperature in CO_2-free system for only few hours at temperature above 1100°C as previously reported in a fair number of studies (Demouchy and Mackwell, 2003; Zhao et al., 2004; Grant et al., 2007; Lemaire et al., 2004; Sokol et al., 2013a, 2013b; Bali et al., 2008; Yang et al., 2014). The only high absorbance IR peaks present are linked to hydrous minerals (brucite and/or serpentine), and are most likely the result of crystallization during the rapid pressure and temperature quench.

The experiments reported here were set up to test if a model CO_2-H_2O-rich kimberlitic liquid could hydrate mantle-derived olivine during its transport toward the surface. The absence of dehydration profile in olivine crystals transported by kimberlites in natural settings, as well as the high water contents reported in mantle-derived olivine from the cratonic settings could be the consequence of hydration, which took place at depths during rapid transport (Baptiste et al, 2012; Bell et al. 2004; Doucet et al., 2014; Kamenetsky et al., 2008; Kurosawa et al., 1997; Miller et al. 1987). In all the experiments reported here, significant OH was not found in the single crystal of forsterite, whatever the duration of the experiment.

The solubility of hydroxyl in olivine in a CO_2-free system under water-saturated conditions is usually defined as (following Kohlstedt et al., 1996):

$$C_{OH}(T, P, f_{H_2O}) = A\, f_{H_2O}{}^{n} \exp\left(\frac{-Q+P\Delta V}{RT}\right) \quad \text{eq. 2}$$

where A is a mineral-dependant constant, f_{H2O} is the fugacity of pure water, n is the fugacity exponent which is equal to 1 (e.g., Kohlstedt et al., 1996, Bali et al., 2008), Q is the activation energy, P is the confining pressure, ΔV is the volume change due to H incorporation in the crystalline structure, R is the gas constant, and T the absolute temperature. According to the equation of state of Pitzer and Sterner (1994), at 1 GPa and 1200°C, f_{H2O} of pure water should be equal to 2.06 GPa. According to the hydrogen solubility law applicable to pure forsterite in Bali et al. (2008), and at pressure and temperature of this study as well as water-saturated conditions in a CO_2-free system, the solubility of OH reaches 38 ppm H_2O wt. in forsterite. The run products reported here are far from such high concentration of OH (< 2 ppm H_2O wt.). It is recognized that in mixed fluids, which are, for instance, composed of CO_2 and H_2O (Holloway and Blank, 1994), the fugacity of H_2O is reduced with the addition of CO_2, and vice-versa. Conceivably relevant to the experiments reported here, the simplest interpretation is that despite the high H_2O bulk content (>10 wt.%; Table 1) in the starting kimberlitic liquid, the presence of CO_2 has lowered the H_2O fugacity to such an extent that it has almost completely prohibited hydration of either the forsterite single crystal or the overgrowth (Fig. 5 and 6). According to Duan and Zhang (2006), at 1 GPa and 1200°C in an ideal binary H_2O-CO_2 system, the activity of water is defined as:

$$a_{H_2O} = f_{H_2O}^{mix} / f_{H_2O}^{pure} \quad \text{eq. 3}$$

For X_{CO2} =0.46, a_{H2O} = 0.6220 and a_{CO2} = 0.5233 (Duan and Zhang, 2006). Therefore, f_{H2O} decreases from a value of 2.03 GPa (pure system) down to 1.28 GPa (binary system), while f_{CO2} decreases from 12 .7 GPa down to 6.65 GPa (i.e., CO_2-H_2O fugacity ratio of 5:1). Then, even if CO_2 is not the dominant volatile in relative mole fraction, it is by far the most abundant in a

304 binary vapor mix. It is to be noted that the above calculations are purely for fluid species; and,
305 due to the non-availability of equations of state, the same calculations cannot be performed for
306 dissolved volatile species in kimberlitic liquids. Also, additional dissolved oxides are not likely
307 to severely inverse the relative, dominant interplay between CO_2 and H_2O fugacity in the whole
308 system. The same limitations on quantitative fugacities have been discussed by Yang et al.,
309 (2014) for a multi-volatiles component solubility law, which can be presented as follow:

310 $$C_{OH}\left(T, P, f_{H_2O}^{mix}\right) = B\, a_{H_2O}\, (f_{H_2O}^{pure})^m \quad exp\left(\frac{-Q+P\Delta V}{RT}\right)$$ eq. 4

311 with a_{H2O} being a function of T, P, the mole fraction of CO_2 (XCO_2) and other oxides in the
312 system, and *m* being the new exponent on the pure water fugacity in a complex volatile system.
313 Moreover, despite occurrence of bubbles inside the capsule and during capsules opening, the
314 kimberlitic liquid might not have reached water saturation at this pressure. On the basis of high-
315 pressure, high-temperature crystallization experiments on olivine phenocrysts from a powder
316 with a composition of an exotic erupted kimberlite (from Udachnaya, Siberia; Kamenetsky et al.,
317 2008), the influence of CO_2 on lowering H_2O fugacity in kimberlitic liquids was previously
318 anticipated by Sokol et al. (2013b). Also, recent experimental studies from Gaetani et al. (2014)
319 and Yang et al. (2014) have assessed the effect of CO_2 on lowering H_2O fugacity and the
320 solubility of H in olivine in a melt-free system (i.e., hydrothermal annealing of natural olivine +
321 free H_2O + $NaHCO_3$ or $Ag_2C_2O_4$). However, in these studies (Gaetani et al., 2014; Yang et al.,
322 2014), hydration was not completely inhibited and hydrogen incorporation in olivine was only
323 reduced by a factor 2-3 under a pressure of 1-5 GPa and a temperature of 1100-1300 °C. Thus,
324 the present results extend the ones from Gaetani et al. (2014) and Yang et al. (2014) in iron-
325 bearing olivine (Fo90), to iron-free forsterite and confirm that the presence of CO_2 in the system
326 drastically decrease the hydrogen incorporation of both forsterite and olivine crystals.

Possible interplay between hydrogen diffusion and forsterite growth.

The important forsterite overgrowth is another notable result from the experiments reported here, and was previously reported in CO_2-free hydration experiments (e.g., Kohlstedt et al., 1996; Bali et al., 2008). One may enquire whether there is a link between crystal overgrowth and the lack of significant OH incorporation in the experiments. From over 20 measurements per crystallographic axis on the high resolution SEM images, it was seen that the overgrowth length is on average after 5h at 1250°C: 72 μm parallel to [100] and 102 μm parallel to [001]; and after 23h at 1200°C: 179 μm parallel to [100] and 153 μm parallel to [001]). Such fast crystal growth could compete with ionic diffusion in the crystal. Therefore, diffusion and growth length must be compared. To calculate possible diffusion length, and on the basis of two types of point defects in forsterite, two mechanisms of hydrogen diffusion can be considered. Indeed, hydrogen diffusion is rate limited by Mg-vacancy or by Si-vacancy diffusivity. Also, using the diffusion coefficients determined experimentally (Demouchy and Mackwell, 2003), one can calculate the characteristic distance (x) of hydrogen diffusion in forsterite (i.e., $x = 2 \times (Dt)^{1/2,}$ where D is the diffusion coefficient in m^2/s and t time in s^{-}). Assuming that hydrogen diffusivity is controlled by Mg-vacancy (Demouchy and Mackwell 2003, Padron-Navarta, et al., 2014), for a duration of 5h at 1250°C, it yields a characteristic distance of 263 μm parallel to [100] and 823 μm parallel to [001]; after 23h at 1200°C, the same calculation yields a characteristic length of 419 μm parallel to [100] and 1337 μm parallel to [001]. Therefore, if this mechanism of diffusion is assumed, the characteristic distance of hydrogen diffusion by far exceeds the overgrowth length and should have permitted full hydration of the forsterite overgrowth and notable hydration of the forsterite

single crystal. Assuming hydrogen diffusivity is controlled by Si-vacancy (Padron-Navarta, et al., 2014), which is a slower mechanism of diffusion, calculations for a duration of 5h at 1250°C, yield a characteristic distance of 149 μm and after 23h at 1200°C a length of 174 μm. In this case, the characteristic distance is close to the length of the overgrowth, and therefore, even if the initial forsterite single crystal was not hydrated, the overgrowth should have incorporated significant H (approx. 114 ppm H_2O wt, using polarized IR, equivalent to 38 ppm H_2O wt, when compared with the same method as in our study: calibration of Paterson and unpolarized IR, see Bali et al., 2008 for details). All available hydrogen diffusion data and solubility experiments converge toward efficient hydrogen incorporation in a CO_2-free system. Except for the drastic reduction of water fugacity in this study, the only remaining possibility to explain the lack of hydration would be an extremely slow diffusivity of hydrogen, on the order of 1 to 5×10^{-15} m^2s^{-1}. Incorporation of Ca in the forsterite overgrowth and euhedral forsterite crystals could also have inhibited H incorporation, but not in the forsterite single crystal (Ca diffusion is slower than H diffusion; Chakraborty, 2010). It would also imply an unrealistic low vacancy concentration in forsterite for annealing experiments at such high temperatures.

Estimation of forsterite growth rate

Furthermore, the crystallization experiments in this study allow estimation of the rate of grain growth of forsterite crystals. In silicate systems with crystals and liquid at chemical equilibrium (with very small ΔT), Ostwald ripening (Ostwald, 1901) allows growth of large grains at the expense of the small ones and layer growth mechanism should control grain growth

instead of continuous growth (Cabane et al., 2005). Following the relation linking grain size and time as (e.g., Ardell, 1972; Kirkpatrick, 1975; Cabane et al., 2005):

$$d^n - d_o^n = kt,$$

where d and d_o are the final and initial grain size, respectively, n the grain growth exponent, k the growth rate and t time. For diffusion-control or spiral layer-growth control (i.e., screw dislocation based), the n exponent is equal to 3 (e.g., Cabane et al., 2005). When applied to experiments in this study, at 1250°C (VB12), calculations yield a growth rate k of $2.34 \times 10^8 \pm 0.90 \times 10^8$ μm^3/h for the [100] axis and $2.28 \times 10^8 \pm 1.14 \times 10^8$ μm^3/h for the [001] axis. At 1200°C (VB6), it yields a growth rate k of $1.34 \times 10^8 \pm 0.41 \times 10^8$ μm^3/h for the [100] axis and of $0.69 \times 10^8 \pm 0.29 \times 10^8$ μm^3/h for the [001] axis. Several studies on grain growth experiments in nano-scale monocrystalline aggregates (melt-free) reported generally slower forsterite (Fo_{100}) growth rates than in the present study (with n determined to be equal to 4 in Ohuchi and Nakamura 2007a, 2007b; Hiraga et al. 2010). Ohuchi and Nakamura (2007a, 2007b) obtained fast growth rates on dry and wet forsterite aggregates (2.29×10^4/h and 6.31×10^3 μm^4/h, respectively) at similar pressure and temperature (1.2 GPa, 1200°C). At lower pressure and higher temperature (1-atm, 1380°C), Hiraga et al. (2010) measured slower growth rates (36 μm^4/h) from grain growth experiments on dry nano forsterite monominerallic aggregates (50 nm to 6 μm). Finally, grain growth experiments on dry nano forsterite plus 5%-enstatite aggregates conducted by Tasaka and Hiraga (2013) at similar pressure and temperatures (1-atm, 1260-1380°C) resulted in growth rates (1.3-34.4 μm^4/s) of the same order of magnitude as in Hiraga et al. (2010). In the olivine-basalt systems, based on the extrapolation of Cabane et al. (2005) and their experimental data, forsterite grain should grow by 5.79 and 9.45 μm after 5h and 23h, respectively. In the forsterite-kimberlite system studied here, the forsterite single crystal grew

more than ten times faster than the estimates from Cabane et al. (2005) for the same duration, emphasizing the potential role of volatiles (here CO_2 and H_2O) on the depolymerization of the melt and its enhancing effect on the grain growth kinetics. Finally, the length of forsterite overgrowth reported here, is similar to the one observed around euhedral olivine (xenocrysts and phenocrysts) transported by kimberlite lavas from Greenland (<0.1-0.2 mm, Arndt et al., 2010). This observation on natural samples indicates very short duration of olivine residence and transport in kimberlite lavas, and thus, very rapid ascent rate of kimberlite lavas from depth >150 km.

Implications

At the scale of point defects, despite the simplified system under consideration, the results of this study emphasize the complex and rather interesting interplay between mixed volatiles (here CO_2 and H_2O) and their incorporation in the crystalline lattice of nominally anhydrous minerals. The results point to the necessity to adjust with care the amount of the respective volatiles when quantification for 'water capacity' or 'CO_2 capacity' for the deep Earth is attempted, since significant hydration (> 100 ppm H_2O wt) at pressure relevant for the lithospheric mantle (1-3 GPa) seems to take place in a CO_2-poor system only.

At larger scale, the main consequence from this experimental study is that the high concentrations of OH measured in mantle-derived olivine from deep peridotites in cratonic settings must be representative of the mantle hydrogen concentration at depth (i.e., for instance, garnet stability field). The concentrations of OH also seem to be unaffected (in-take or out-take) by their transport in kimberlitic liquids from depths. Therefore, the high concentrations of OH in

Kaapvaal craton xenoliths as reported by Baptiste et al. (2012) were likely acquired during their mantle history, and were further controlled by metasomatism (Baptiste et al., 2012).

Acknowledgements

This study was financially supported by the ANR JCJC "HyDeep" awarded to NBC and also with partial support from FP7-PEOPLE-2011-CIG (#303301) "GOBMEUM" and the Deep Carbon Observatory (Diamonds and Mantle Geodynamics project) awarded to SK. The authors thank two anonymous referees and Journal Associate Editor for their comments on the manuscript. C. Nevado and D. Delmas are thanked for providing high-quality thin sections for SEM–EBSD. David Troadec is thanked for providing high-quality FIB thin sections for TEM. For the generous supply of magnesite from Oberdorf, SK thanks Peter Ulmer (ETH, Zürich). The FIB facility at the Institut d'électronique, de microélectronique et de nanotechnologie is supported by Université Lille 1, the Centre National de la Recherche Scientifique (CNRS, France), and the Conseil Régional du Nord-Pas de Calais (France). The TEM in Lille and EBSD-SEM in Montpellier are both national facilities and are supported by the Institut National de Sciences de l'Univers (INSU) from the CNRS, France, as well as the Conseil Régional Languedoc-Roussillon (France), the Conseil Regional du Nord-Pas de Calais, and the European Regional Development Fund (ERDF).

References

Ackermand D., Seifert, F., Schreyer, W., (1975) Instability of sapphirine at high-pressure. Contributions to Mineralogy and Petrology 50, 79-92.

Ardell, A.J. (1972) On the coarsening of grain boundary precipitates. Acta Metallurgica 20, 601-609.

Arndt, N.T., Guitreau, M., Boullier, A.-M., Le Roex, A.P., Tommasi, A., Cordier, P., Sobolev, A. (2010) Olivine, and the origin of kimberlite. Journal of Petrology 51, 573-602.

Bali, E., Bolfan-Casanova, N., Koga, K., (2008) Pressure and temperature dependence of H solubility in forsterite: an implication to water activity in the Earth interior. Earth and Planetary Science Letters 268, 354–363.

Baptiste, V., Tommasi, A., and Demouchy, S. (2012) Deformation and hydration of the lithospheric mantle beneath the Kaapvaal craton, South Africa. Lithos 149, 31-50.

Becker, M., and Le Roex, A.P. (2006) Geochemistry of South African on- and off-craton, group I and group II kimberlites: Petrogenesis and source region evolution. Journal of Petrology 47, 673-703.

Bell, D.R., Rossman, G.R., and Moore, R.O. (2004) Abundance and Partitioning of OH in a High-pressure Magmatic System: Megacrysts from the Monastery Kimberlite, South Africa. Journal of Petrology, 45, 1539-1564.

Bolfan-Casanova, N., Keppler, H., Rubie, D.C., 2000. Water partitioning between nominally anhydrous minerals in the MgO-SiO2-H2O system up to 24 GPa: Implications for the

460 distribution of water in the Earth's mantle. Earth and Planetary Science Letters 182, 209–
461 221.

462 Brooker, R.A., Sparks, R.S.J., Kavanagh, J.L., Field, M., (2011). The volatile content of
463 hypabyssal kimberlite magmas: some constraints from experiments on natural rock
464 compositions. Bulletin of Volcanology 73, 959–981.

465 Buob, A., Luth, R.W., Schmidt, M.W., and Ulmer, P. (2006) Experiments on CaCO3-MgCO3
466 solid solutions at high pressure and temperature. American Mineralogist 91, 435-440.

467 Cabane, H., Laporte, D., and Provost, A. (2005) An experimental study of Ostwald ripening of
468 olivine and plagioclase in silicate melts: implications for the growth and size of crystals in
469 magmas. Contributions to Mineralogy and Petrology, 150, 37-53.

470 Chakraborty, S. (2010) Diffusion coefficients in olivine, wadsleyite and ringwoodite, in
471 Diffusion in Minerals and Melts, Reviews in Mineralogy and Geochemistry, 72, eds. Y.
472 Zhang and D. Cherniak, 603-639, doi: 10.2138/rmg.2010.72.13.

473 Dalton, J.A., and Presnall, D.C. (1998) The continuum of primary carbonatitic kimberlitic melt
474 compositions in equilibrium with lherzolite: Data from the system CaO-MgO-Al_2O_3-SiO_2-
475 CO_2 at 6GPa. Journal of Petrology, 39, 1953-1964.

476 Deer, W.A., Howie, R.A., Zussman, J., (1992). An introduction to the Rock-forming minerals.,
477 2nd ed. The Geological Society. London.

478 Demouchy, S., Ishikawa A., Tommasi A., Alard, O. and Keshav S. (2015) Characterisation of the
479 hydration in the oceanic mantle lithosphere: peridotite xenoliths from Ontong Java Plateau
480 as an example. Lithos 212-215:189-201.

481 Demouchy, S., and Mackwell, S.J. (2003) Water diffusion in synthetic iron-free forsterite.
482 Physics and Chemistry of Minerals 30, 786-794.

483 Demouchy, S., Mackwell, S., (2006). Mechanisms of hydrogen incorporation and diffusion in
484 iron-bearing olivine. Physics and Chemistry of Minerals 33, 347–355.

485 Demouchy, S., Tommasi, A., Barou, F., Mainprice, D., and Cordier, P. (2012) Deformation of
486 olivine in torsion under hydrous conditions. Physics of the Earth and Planetary Interiors
487 202-203, 56-70.

488 Demouchy, S., Mainprice, D., Tommasi, A., Couvy, H., Barou, F., Frost, D.J., and Cordier, P.
489 (2011) Forsterite to wadsleyite phase transformation under stress and consequences for the
490 Earth's mantle transition zone. Physics of the Earth and Planetary Interiors 184, 91-104.

491 Doucet, L.-S., Peslier, A.H., Ionov, D.A., Brandon, A.D., Golovin, A.V., Goncharov, A.G., and
492 Ashchepkov, I.V. (2014) High water contents in the Siberian cratonic mantle linked to
493 metasomatism: an FTIR study of Udachnaya peridotite xenoliths. Geochimica et
494 Cosmochimica Acta 137, 159-187.

495 Duan, Z.H., Zhang, Z.G. (2006) Equation of state of the H_2O-CO_2 system up to 10 GPa and
496 2573K: Molecular dynamics simulations with ab initio potential surface. Geochimica et
497 Cosmochimica Acta 70, 2311-2324.

498 Gaetani, G.A., O'Leary, J.A., Koga, K.T., Hauri, E.H., Rose-Koga, E.F., Monteleone, B.D.,
499 (2014). Hydration of mantle olivine under variable water and oxygen fugacity conditions.
500 Contributions to Mineralogy and Petrology 167, 965.

501 Gaetani, G.A., and Grove, T.L. (1998) The influence of water on melting of mantle peridotite.
502 Contributions to Mineralogy and Petrology 131, 323-346.

503 Grant, K., Ingrin, J., Lorand, J.P., Dumas, P., (2007). Water partitioning between mantle minerals
504 from peridotite xenoliths. Contributions to Mineralogy and Petrology 154, 15–34.

505 Gudfinnsson, G.H., and Presnall, D.C. (2005) Continuous gradations among primary carbonatitic,
506 kimberlitic, melilitic, basaltic, picritic, and komatiitic melts in equilibrium with garnet
507 lherzolite at 3-8 GPa. Journal of Petrology 46, 1645-1659.

508 Hiraga, T., Tachibana, C., Ohashi, N., and Sano, S. (2010) Grain growth systematics for forsterite
509 ± enstatite aggregates: Effect of lithology on grain size in the upper mantle. Earth and
510 Planetary Science Letters 291, 10-20.

511 Hirth, G., and Kohlstedt, D.L. (1996) Water in the oceanic upper mantle: Implications for
512 rheology, melt extraction, and the evolution of the lithosphere. Earth and Planetary Science
513 Letters 144, 93-108.

514 Holloway, J.R., and Blank, J.G. (1994) Application of experimental results to C-O-H species in
515 natural melts. In Mineralogical Society of America Reviews in Mineralogy 30, 187-230.

516 Jacobsen, S.D., Jiang, F., Mao, Z., Duffy, T.S., Smyth, J.R., Holl, C.M., and Frost, D.J. (2008)
517 Effects of hydration on the elastic properties of olivine. Geophysical Research Letters 35,
518 L14303.

519 Kamenetsky, V.S., Kamenetsky, M.B., Sobole, A.V., Golovin, A.V., Demouchy, S., Faure, K.,
520 Sharygin, V.V., Kuzmin, D.V., (2008). Olivine in the Udachnaya-East Kimberlite (Yakutia,
521 Russia): Types, compositions and origins. Journal of Petrology 49, 823–839.

Karato, S. (1990) The role of hydrogen in the electrical conductivity of the upper mantle. Nature, 347, 272-273.

Keppler, H. (2003) Water solubility in carbonatite melts. American Mineralogist 88, 1822-1824.

Keppler, H., and Rauch, M. (2000) Water solubility in nominally anhydrous minerals measured by FTIR and HNMR. Physics and Chemistry of Minerals 27, 371-376.

Kikuchi, S. (1928) Diffraction of cathode rays by mica. Japanese Journal of Physics, 5, 83-96.

Kirkpatrick, R.J. (1975) Crystal growth from the melt: A review. American Mineralogist 60, 798-814.

Kjarsgaard, B.A., Pearson, D.G., Tappe, S., Nowell, G.M., and Dowall, D.P. (2009) Geochemistry of hypabyssal kimberlites from Lac de Gras, Canada: Comparisons to a global database and applications to the parent magma problem. Lithos 112S, 236-248.

Kohlstedt, D.L., Keppler, H., and Rubie, D.C. (1996) Solubility of water in the alpha, beta, and Y phases of (Mg, Fe)2SiO4. Reviews in Mineralogy & Geochemistry 123, 345-357.

Kurosawa, M., Yurimoto, H., and Sueno, S. (1997) Patterns in the hydrogen and trace element compositions of mantle olivines. Physics and Chemistry of Minerals 24, 385-395.

Lemaire, C., Kohn, S.C., and Brooker, R. (2004) The effect of the silica activity on the incorporation mechanisms of water in synthetic forsterite: a polarized spectroscopic study. Contributions to Mineralogy and Petrology 147, 48-57.

Mackwell, S.J., Kohlstedt, D.L., and Paterson, M.S. (1985) The role of water in the deformation of olivine single-crystals. Journal of Geophysical Research-Solid Earth and Planets 90, 1319-1333.

Matsyuk, S.S., and Langer, K. (2004) Hydroxyl in olivines from mantle xenoliths in kimberlites of the Siberian platform. Contributions to Mineralogy and Petrology 147, 413-437.

Matsyuk, S.S., Langer, K., and Hösch, A. (1998) Hydroxyl defects in garnets from mantle xenoliths in kimberlites of the Siberian platform. Contributions to Mineralogy and Petrology 132, 163-179.

Matveev, S., and Stachel, T. (2007) FTIR spectroscopy of OH in olivine: A new tool in kimberlite exploration. Geochimica et Cosmochimica Acta 71, 5528-5543.

Miller, G.H., Rossman, G.R., and Harlow, G.E. (1987) The natural occurrence of hydroxide in olivine. Physics and Chemistry of Minerals 14, 461-472.

Mitchell, R.H. (1986) Kimberlites: Mineralogy, Geochemistry, and Petrology. 442 p. Plenum Press, New York.

Mitchell, R.H. (1995) Kimberlites, Orangeites, and Related Rocks. 410 p. Plenum Press, New York.

Ohuchi, T., and Nakamura, M. (2007a) Grain growth in the forsterite-diopside system. Physics of the Earth and Planetary Interiors 160, 1-21.

Ohuchi, T., and Nakamura, M. (2007b) Grain growth in the system forsterite-diopside-water. Physics of the Earth and Planetary Interiors 161, 281-304.

Ostwald, W. (1901) Uber die vemeintliche Isomerie des roten und gelben Quecksilberoxyds und die Oberflachen-spannung Fester Korper. Zeitschrift für Physikalische Chemie 34, 495-512.

Padrón-Navarta, J.A., Hermann, J., and O'Neill, H. (2014) Site-specific hydrogen diffusion rates in Forsterite. Earth and Planetary Science Letters 392, 100-112.

Paterson, M.S. (1982) The determination of hydroxyl by infrared absorption in quartz, silicate glasses and similar materials. Bulletin de Minéralogie 105, 20-29.

Peslier, A.H. (2010) A review of water contents of nominally anhydrous natural minerals in the mantles of Earth, Mars and the Moon. Journal of Volcanology and Geothermal Research 197, 239-258.

Peslier, A.H., Woodland, A.B., Bell, D.R., and Lazarov, M. (2010) Olivine water contents in the continental lithosphere and the longevity of cratons. Nature 467, 78–81.

Pitzer, K.S., Sterner, S.M. (1994) Equations of state valid continuously from zero to extreme pressures for H_2O and CO_2. Journal of Chemical Physics 101, 3111–3116.

Smith, C.B., Allsopp, H.L., Kramers, J.D., Hutchison, G., and Roddick, J.C. (1985a) Emplacement ages of Jurassic-Cretaceous South African kimberlites by the Rb-Sr method on phlogopite and whole-rock samples. South African Journal of Geology 88, 249-266.

Smith, C.B., Gurney, J.J., Skinner, E.M.W., Clement, C.R., and Ebrahim, N. (1985b) Geochemical character of Southern African kimberlites; a new approach based on isotopic constraints. South African Journal of Geology 88, 267-280.

580 Sokol, A.G., Kupriyanov, I.N., and Palyanov, Y.N. (2013a) Partitioning of H_2O between olivine
581 and carbonate-silicate melts at 6.3 GPa and 1400°C: Implications for kimberlite formation.
582 Earth and Planetary Science Letters 383, 58-67.

583 Sokol, A.G., Kupriyanov, I.N., Palyanov, Y.N., Kruk, A.N., and Sobolev, N.V. (2013b) Melting
584 experiments on the Udachnaya kimberlite at 6.3-7.5GPa: Implications for the role of H_2O
585 in magma generation and formation of hydrous olivine. Geochimica et Cosmochimica Acta
586 101, 133-155.

587 Sparks, R.S.J., Brooker, R.A., Field, M., Kavanagh, J., Schumacher, J.C., Walter, M.J., and
588 White, J. (2009) The nature of erupting kimberlite melts. Lithos 112, 429-438.

589 Tasaka, M., and Hiraga, T. (2013) Influence of mineral fraction on the rheological properties of
590 forsterite + enstatite during grain-size-sensitive creep: 1. Grain size and grain growth laws.
591 Journal of geophysical Research (Solid Earth), 118, 1-21.

592 Xirouchakis, D., Hirschmann, M.M., and Simpson, F. (2001) The effect of titanium on the silica
593 content and on mineral-liquid partitioning of mantle-equilibrated melts. Geochimica et
594 Cosmochimica Acta 65, 2201-2217.

595 Yang, X., Dingding, L., and Xia, Q. (2014) CO_2-induced small water solubility in olivine and
596 implications for properties of the shallow mantle. Earth and Planetary Science Letters 403,
597 37-47.

598 Zhao, Y.H., Ginsberg, S.B., Kohlstedt, D.L., 2004. Solubility of hydrogen in olivine: dependence
599 on temperature and iron content. Contributions to Mineralogy and Petrology 147, 155–161.

600

601

602

603

604 **Figure captions**

605 Figure 1: Schematic illustration of the capsule assembly for high pressure diffusion experiments.

606

607 Figure 2: SEM-images of the run VB12 after experiment, showing (a) the entire capsule section
608 with the forsterite single crystal displaying a well-defined overgrowth, (b) the forsterite single
609 crystal boundary, its overgrowth, and the surrounding euhedral forsterites, (c) the euhedral
610 forsterite and the carbonate phase are circled by a white line, (d) the forsterite single crystal
611 boundary, its overgrowth, and the surrounding euhedral forsterites (e) Spinel (indicated by
612 arrows) within the forsterite overgrowth and in contact with the euhedral grains of forsterite.

613

614 Figure 3: SEM images of VB12 and electron back-scattered diffraction patterns (Kikuchi's
615 bands; Kikuchi, 1928) of (a) the forsterite single crystal, (b) the forsterite overgrowth, (c) a
616 euhedral forsterite, (d) the Al-rich phase, (e) the Ca-rich phase.

617

618 Figure 4: TEM images of the run VB6 showing (a) euhedral nano-scale phases in the forsterite
619 overgrowth (TEM Bright field), (b) EXD chemical maps (200x200 pixels, acquired in the STEM
620 mode with a 500 ms dwell time) combining Al (yellow) + Si (green) + Ca (blue) identifying Al-

621 rich spinel, Ca-rich phase (carbonate), and the forsterite matrix, respectively, (c) precession (2.5°)
622 electron diffraction pattern along the [100] axis for Al-rich spinel, [010] and [001] are indexed in
623 the image. Abbreviations are: Fo: Forsterite, Sp: spinel, Carb: carbonate

624

625 Figure 5: Unpolarized infrared spectra of the forsterite crystals after experiments (at 1 GPa) from
626 this study. FTIR spectrum from olivine in Kaapvaal xenoliths (transported by kimberlite, Baptiste
627 et al., 2012), in Malaita xenoliths (transported by alnoites, Demouchy et al., 2015), and in
628 synthetic forsterite single crystals during diffusion experiments in a piston-cylinder experiments
629 at variable temperature, pressure conditions, and for different duration (Demouchy and
630 Mackwell, 2003) are presented for comparison. All spectra are normalized to a sample thickness
631 of 1 cm. Star indicates peaks attributed to serpentine.

632

633 Figure 6: Unpolarized FTIR profile across the forsterite single crystal interface after the
634 experiment, VB6. Six spectra were measured with a step size of 30 μm. All spectra are
635 normalized to a sample thickness of 1 cm. Stars indicate peaks attributed to serpentine, see main
636 text for details on OH band attribution.

637

638

639

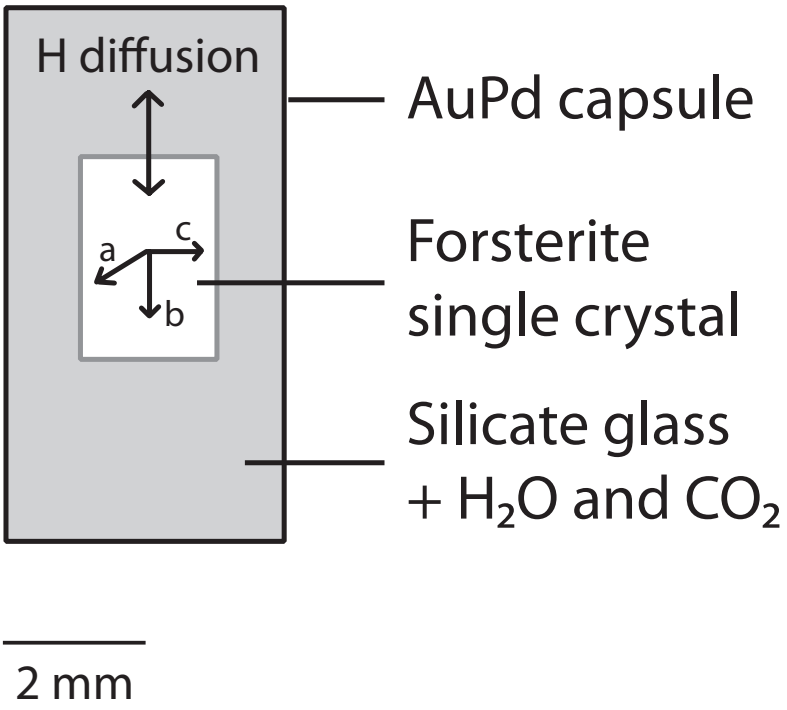

Baptiste et al.
Figure 1

This is a preprint, the final version is subject to change, of the American Mineralogist (MSA)
Cite as Authors (Year) Title. American Mineralogist, in press.
(DOI will not work until issue is live.) DOI: http://dx.doi.org/10.2138/am-2015-5200

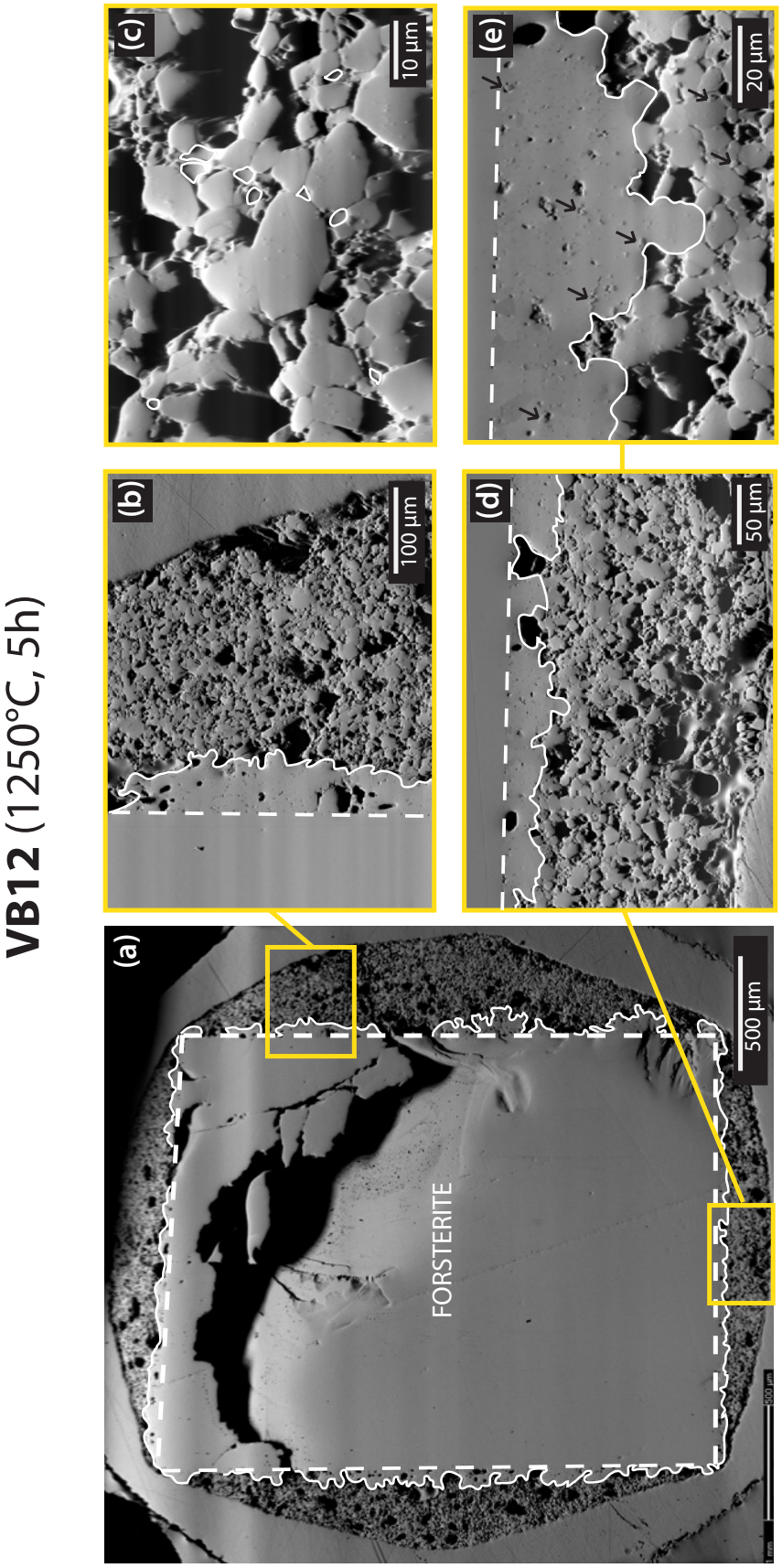

Baptiste et al
Figure 2

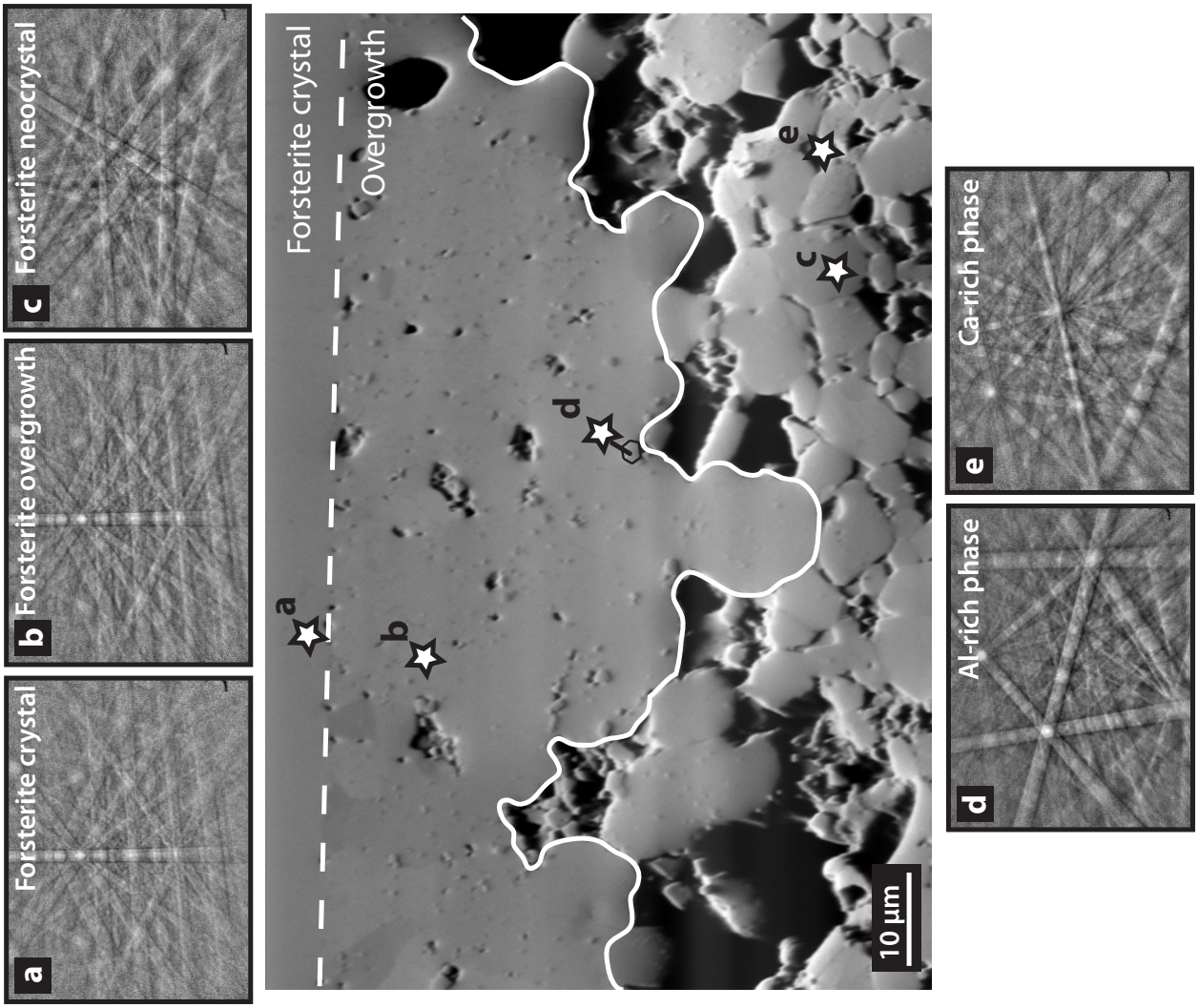

Baptiste et al
Figure 3

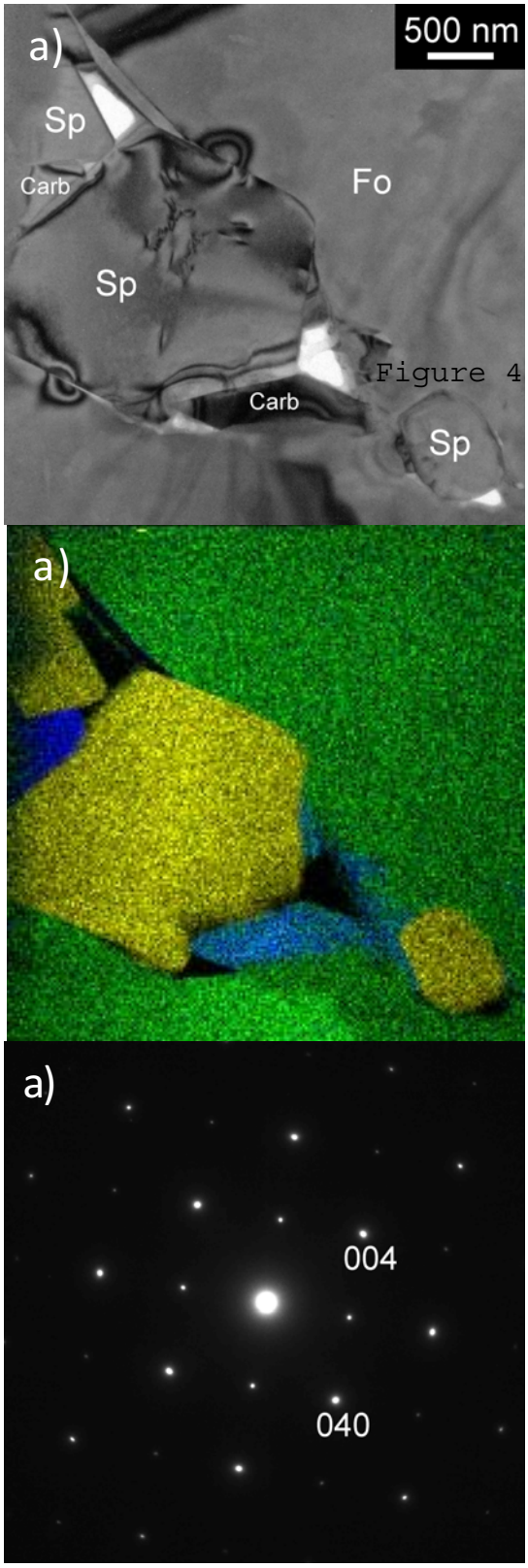

Figure 4

aa tiste et al
a) tise 4

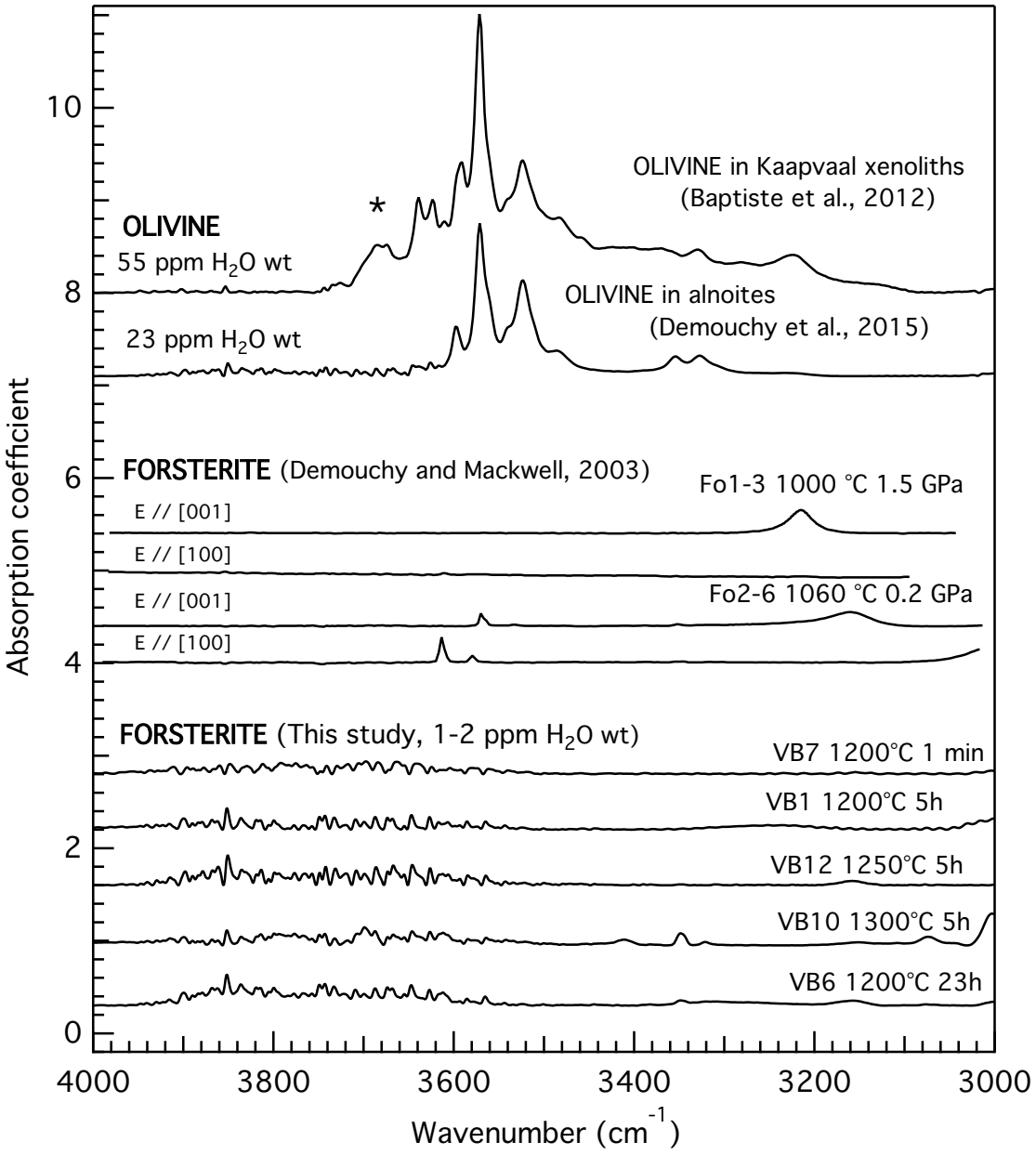

Baptiste et al
Figure 5

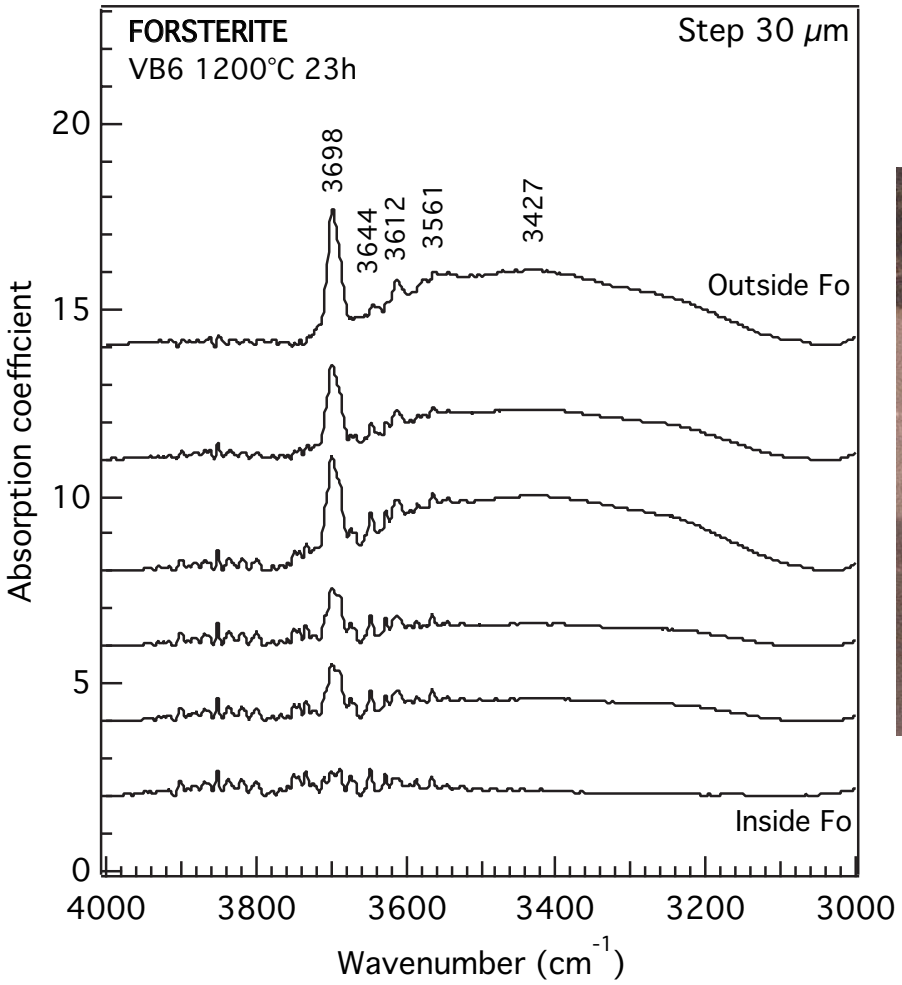

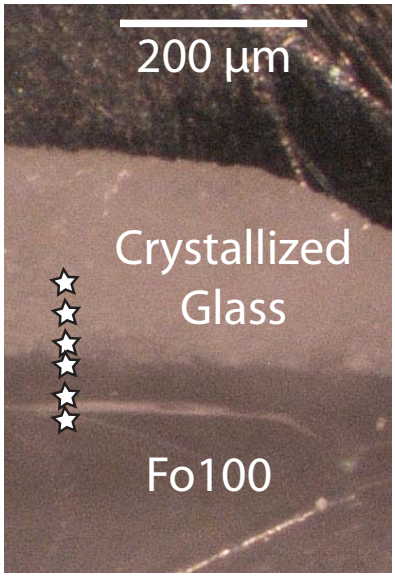

Baptiste et al
Figure 6

Table 1: Forsterite and starting material composition, average kimberlite group-I and group-II compositions, and compositions of run products from VB12.

					VB12 compositions (after run)				
Wt.%	**Starting composition**	**Group I Kimberlite Average***	**Group II Kimberlite Average***	**Forsterite crystal composition**	Fo single crystal	Fo overgrowth	Fo neocrystals	Al-rich phase	Ca-rich phase
SiO_2	30	26.15	33.89	44.76	43.25	43.02	43.08	4.73	28.35
TiO_2	0	2.58	1.77	0.00	0.01	0.00	0.00	0.00	0.03
Al_2O_3	4	2.76	3.76	0.01	0.02	0.46	1.21	53.37	1.78
FeO		-	-	0.00	-0.01	0.00	0.00	0.16	0.05
Fe_2O_3	0	10.72	8.76	-	-	-	-	-	-
MnO	0	0.19	0.18	0.00	0.01	0.00	0.00	0.00	0.01
MgO	28	25.20	23.15	55.41	56.49	54.61	54.99	25.04	18.86
CaO	14	13.20	9.96	0.00	0.00	0.43	0.31	10.20	28.75
Na_2O	0	0.16	0.25	-0.01	0.00	0.00	0.00	0.01	0.02
K_2O	0	0.83	3.63	0.00	0.00	0.00	0.00	0.01	0.00
P_2O_5	0	2.04	1.85	-	-	-	-	-	-
SO_3	0	0.17	0.21	-	-	-	-	-	-
NiO	0	0.11	0.14	0.00	0.01	0.00	0.00	0.01	0.00
Cr_2O_3	0	0.18	0.23	-0.01	0.00	0.00	0.00	0.00	0.00
LOI		14.71	10.75						
H_2O-	-	0.27	1.34	-	-	-	-	-	-
H_2O+	-	6.67	7.33	-	-	-	-	-	-
H_2O	13	-	-	-	-	-	-	-	-
CO_2	11	8.19	4.21	-	-	-	-	-	-
total		84.29	87.78	100.16	99.78	98.51	99.60	93.53	77.85

* Average compositions from Becker and Le Roex (2006).
Fo:single crystal of crystallographically oriented forsterite

Table 2: Experimental conditions in piston-cylinder and OH concentration in forsterite after run

Run	Sample	Pressure (GPa)	Temperature (°C)	Duration (min)	free fluid	OH concentration (after run) (ppm H2O wt)
1	VB7	1.0	1200	1	✔	1
2	VB1	1.0	1200	300	✔	2
3	VB6	1.0	1200	1380	✔	2
4	VB10	1.0	1300	300	✔	2
5	VB12	1.0	1250	300	✔	2